Medical Science Series

THE PHYSICS OF MEDICAL IMAGING

Edited by

Steve Webb

Joint Department of Physics,
Institute of Cancer Research and
Royal Marsden Hospital, Sutton, Surrey

Adam Hilger, Bristol and Philadelphia

CHAPTER 4

X-RAY TRANSMISSION COMPUTED TOMOGRAPHY

W SWINDELL AND S WEBB

4.1 THE NEED FOR SECTIONAL IMAGES

When we look at a chest x-ray (see figure 4.1), certain anatomical features are immediately apparent. The ribs, for example, show up as a light structure because they attenuate the x-ray beam more strongly than the surrounding soft tissue, so the film receives less exposure in the shadow of the bone. Correspondingly, the air-filled lungs show up as darker regions.

Figure 4.1 Typical chest x-radiograph.

A simple calculation illustrates the type of structure that one could expect to see with this sort of conventional transmission radiograph. The linear attenuation coefficients for air, bone, muscle and blood are

$$\mu_{air} = 0$$
$$\mu_{bone} = 0.48\ cm^{-1}$$
$$\mu_{muscle} = 0.180\ cm^{-1}$$
$$\mu_{blood} = 0.178\ cm^{-1}$$

for the energy spectrum of a typical diagnostic x-ray beam. Thus, for a slab of soft tissue with a 1 cm cavity in it, the results of table 4.1 follow at once using Beer's expression for the attenuation of the primary beam, namely

$$I(x) = I_0 \exp(-\mu x). \tag{4.1}$$

Table 4.1 Contrast in a transmission radiograph.

Material in cavity	$I(x)/I_0$ (x = 1 cm)	Difference (%) with respect to muscle
Air	1.0	+20
Blood	0.837	+ 0.2
Muscle	0.835	0
Bone	0.619	−26

X-ray films usually allow contrasts of the order of 2% to be seen easily, so a 1 cm thick rib or a 1 cm diameter air-filled trachea can be visualised. However, the blood in the blood vessels and other soft-tissue details, such as details of the heart anatomy, cannot be seen on a conventional radiograph. In fact, to make the blood vessels visible, the blood has to be infiltrated with a liquid contrast medium containing iodine compounds; the iodine temporarily increases the linear attenuation coefficient of the fluid medium to the point where visual contrast is generated (see §3.8.1, where contrast media are discussed in detail). Consideration of photon scatter further degrades contrast (see §§2.4.1 and 3.6.1).

Another problem with the conventional radiograph is the loss of depth information. The three-dimensional structure of the body has been collapsed, or projected, onto a two-dimensional film and, while this is not always a problem, sometimes other techniques such as stereoscopic pairs of radiographs or conventional tomography (see §3.3.1) are needed to retrieve the depth information. Some early history of conventional tomography is provided by MacDonald (1981), and different geometries and equipment are reviewed by Coulam *et al* (1981).

It is apparent that conventional x-radiographs are inadequate in these two respects, namely the inability to distinguish soft tissue and the inability to resolve spatially structures along the direction of x-ray propagation.

4.2 THE PRINCIPLES OF SECTIONAL IMAGING

With computed tomography, a planar slice of the body is defined and x-rays are passed through it only in directions that are contained within, and are parallel to, the plane of the slice (see figure 4.2). No part of the body that is outside of the slice is interrogated by the x-ray beam, and this eliminates the problem of 'depth scrambling'. The CT image is as though the slice (which is usually a few millimetres thick) had been physically removed from the body and then radiographed by passing x-rays through it in a direction perpendicular to its plane. The resulting images show the human anatomy in section with a spatial resolution of about 1 mm and a density (linear attenuation coefficient) discrimination of better than 1% (see figure 4.3). This chapter is about the method of converting the x-ray measurements of figure 4.2 into the image shown in figure 4.3.

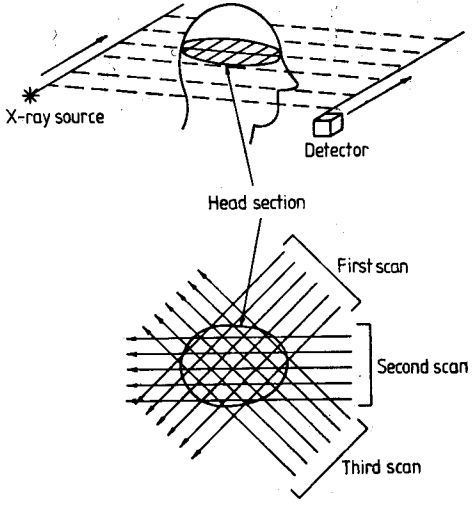

Figure 4.2 Simple scanning system for transaxial tomography. A pencil beam of x-rays passes through the object and is detected on the far side. The source–detector assembly is scanned sideways to generate one projection. This is repeated at many viewing angles and the required set of projection data is obtained. (Reproduced from Barrett and Swindell (1981).)

There are many good reviews on the subject of computed tomography: see, for example, Brooks and Di Chiro (1975, 1976), Kak (1979) and Zonneveld (1979). The commercial development of x-ray computed tomography has been described as the most important breakthrough in diagnostic radiology since the development of the first planar radiograph.

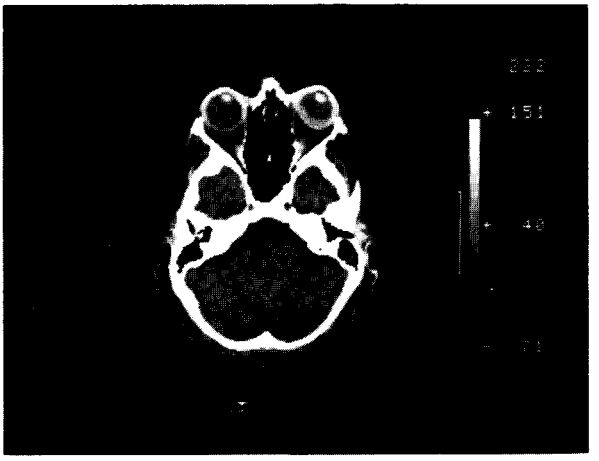

(*a*)

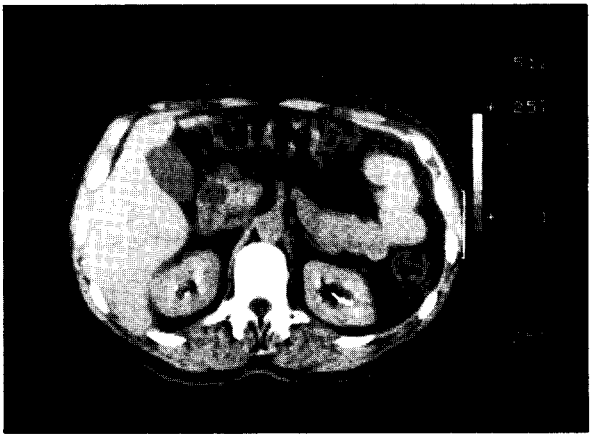

(*b*)

Figure 4.3 (*a*) CT image of a head taken at eye level. (*b*) Abdominal section through the kidneys.

4.2.1 Scanner configurations

As far as the patient is concerned, the CT scanner is a machine with a large hole in it. The body or the head is placed inside the hole in order to have the pictures taken (see figure 4.4). The covers of the machine hide a complicated piece of machinery, which has evolved through several versions since its inception (Hounsfield 1973). Here follows a short description of this development.

A finely collimated source defines a pencil beam of x-rays, which is then measured by a well collimated detector. This source–detector combination measures parallel projections, one sample at a time, by

stepping linearly across the patient. After each projection, the gantry rotates to a new position for the next projection (see figure 4.5). Since there is only one detector, calibration is easy and there is no problem with having to balance multiple detectors; also costs are minimised. The scatter rejection of this first-generation system is higher than that of any other generation because of the two-dimensional collimation at both source and detector. The system is slow, however, with typical acquisition times of 4 min per section, even for relatively low-resolution images.

Figure 4.4 Typical CT scanner.

Data gathering was speeded up considerably in the second generation. Here a single source illuminated a bank of detectors with a narrow (~10°) fan beam of x-rays (see figure 4.6). This assembly traverses the patient and measures N parallel projections simultaneously (N is the number of detectors). The gantry angle increments by an angle equal to the fan angle between consecutive traverses. These machines can complete the data gathering in about 20 s. If the patient can suspend breathing for this period, the images will not be degraded by motion blur, which would otherwise be present in chest and abdominal images.

In third-generation systems, the fan beam is enlarged to cover the whole field of view (see figure 4.7). Consequently, the gantry needs only to rotate, which it can do without stopping, and the data gathering can be done in 4–5 s. It is relatively easy for a patient to remain still for this length of time. Detector balancing is critical for this geometry if circular 'ring' artefacts are to be avoided. Xenon detectors are often chosen because of their stable nature of operation.

Fourth-generation systems use a stationary ring of typically 1000 detectors and only the source rotates (see figure 4.8). Scan speeds remain fast and the ring artefact is overcome. Since every detector is, at some time during the scan, sampling the unattenuated x-ray beam,

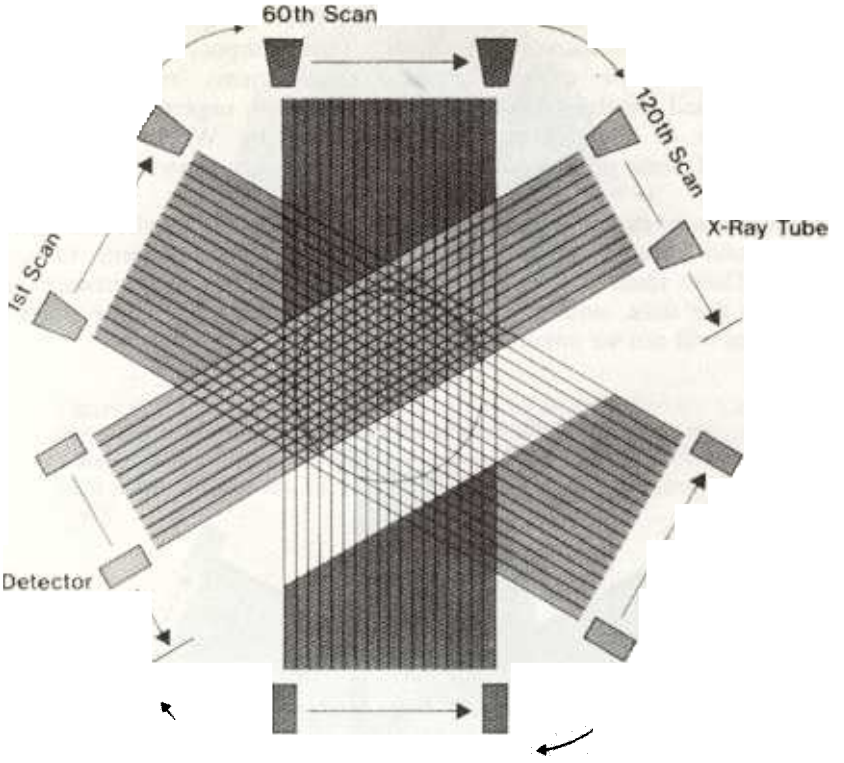

Figure 4.5 Schematic representation of a first-generation CT scanner. It utilises a single pencil beam and single detector for each scan slice. The x-ray source and detector are passed transversely across the object being scanned, with incremental rotations of the system at the end of each transverse motion. (Reproduced from Maravilla and Pastel (1978).)

calibration in 'real time' can be performed.

In the race for speed, the next clinically useful break point comes at around 0.1 s for the data acquisition time. This permits cardiac motion to be frozen. This will allow clearer images not only of the heart but also of organs that are well perfused with blood, such as the liver, and which pulsate in synchrony to the heart beat. Mechanical movement is ruled out and multiple stationary sources are prohibitively cumbersome and expensive. The fifth-generation device (Peschmann *et al* 1985) has no moving parts. A target of the x-ray tube follows the shape of a circular arc of approximately 210°. The patient is placed at the centre of this arc and the effective source of x-rays is made to move by scanning the electron beams around the circumference of the target (see figure 4.9). Scan times can thus be reduced to a few milliseconds.

Special x-ray sources and detectors have been designed and manufactured for use in CT scanners. Each generation imposes its own special requirements. There are also special requirements imposed on the power supplied for the x-ray tubes, especially with regard to stability. A good review of these problems is provided by Webb (1987). The properties of some photon scintillation detectors are shown later in table 6.1.

In addition to the gantry, which houses the scanning mechanism, x-ray sources and detectors, there are other essential components to a CT system. These include the computer, which controls the hardware and processes the data, and the operator's viewing console. These parts of the system will not be covered in this book.

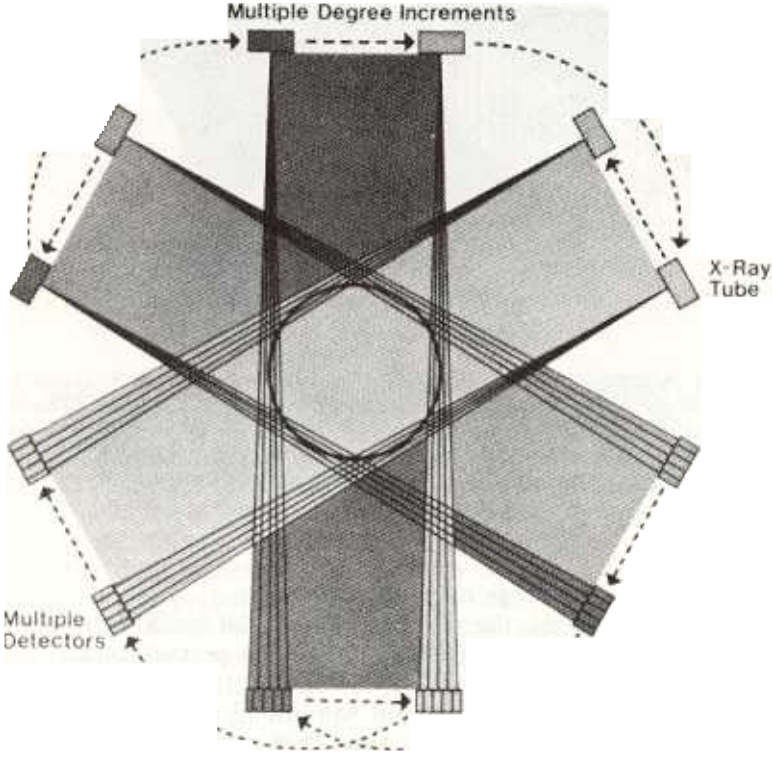

Figure 4.6 Schematic representation of a second-generation CT scanner. A narrow-angle fan beam of x-rays and multiple detectors record several pencil beams simultaneously. As the diverging pencil beams pass through the patient at different angles, this enables the gantry to rotate in increments of several degrees and results in markedly decreased scan times of 20 s or less. (Reproduced from Maravilla and Pastel (1978).)

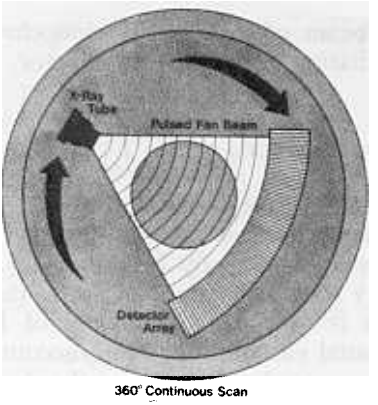

Figure 4.7 Schematic representation of a third-generation CT scanner in which a wide-angle fan beam of x-rays encompasses the entire scanned object. Several hundred measurements are recorded with each pulse of the x-ray tube. (Reproduced from Maravilla and Pastel (1978).)

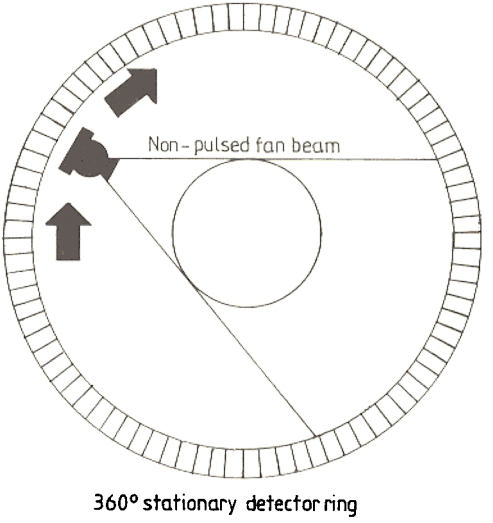

Figure 4.8 Schematic representation of a fourth-generation CT scanner. There is a rotating x-ray source and a continuous 360° ring of detectors, which are stationary. Leading and trailing edges of the fan beam pass outside the patient and are used to calibrate the detectors. (Reproduced from Maravilla and Pastel (1978).)

4.2.2 Line integrals

The data needed to reconstruct the image are transmission measurements through the patient. Assuming, for simplicity, that we have (i) a

very narrow pencil beam of x-rays, (ii) monochromatic radiation and (iii) no scattered radiation reaching the detector, then the transmitted intensity is given by

$$I_\phi(x') = I^0_\phi(x') \exp\left(-\int_{AB} \mu[x, y]\, dy'\right) \tag{4.2}$$

where $\mu[x, y]$ is the two-dimensional distribution of the linear attenuation coefficient, ϕ and x' define the position of the measurement and $I^0_\phi(x')$ is the unattenuated intensity (see figure 4.10). The $x'y'$ frame rotates with the x-ray source position such that the source is on the y' axis. Equation (4.2) is simply an extension of Beer's law (equation (4.1)) to take the spatial variation of μ into account. Frequently $\mu[x, y]$ is simply referred to, somewhat loosely, as the density distribution, and we shall adopt that practice here. In this context, 'density' refers to electron density (electrons/cm^3), which for most practical CT scanners is a parameter found to be related to attenuation coefficient by a series of linear relationships (see e.g. Parker *et al* 1980).

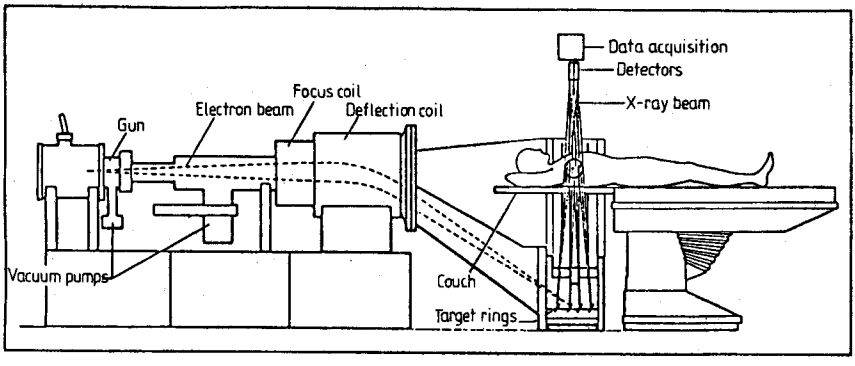

Figure 4.9 Imatron CT-100 ciné CT scanner; longitudinal view. Note the use of four target rings for multislice examination. (Courtesy of Imatron.)

A single projection of the object $\lambda_\phi(x')$ is defined as

$$\begin{aligned}\lambda_\phi(x') &= -\ln[I_\phi(x')/I^0_\phi(x')] \\ &= \int_{-\infty}^{\infty}\int_{-\infty}^{\infty} \mu[x, y]\delta(x\cos\phi + y\sin\phi - x')\, dx\, dy\end{aligned} \tag{4.3}$$

where, now, the Dirac delta function δ picks out the path of the line integral, since the equation of AB is $x' = x\cos\phi + y\sin\phi$.

Equation (4.3) expresses the linear relationship between the object function $\mu[x, y]$ and the measured projection data λ_ϕ. The problem of reconstructing is precisely that of inverting equation (4.3), i.e. recovering $\mu[x, y]$ from a set of projections $\lambda_\phi(x')$.

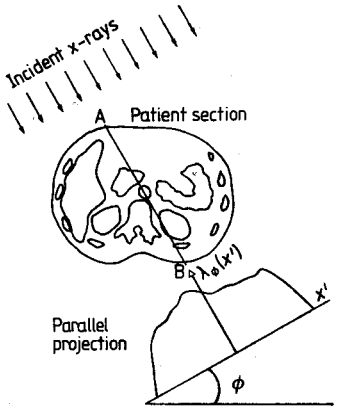

Figure 4.10 Projections are defined as the negative logarithm of the fractional x-ray transmittance of the object, $\lambda_\phi(x') = -\ln[I_\phi(x')/I^0_\phi(x')]$. ϕ is the angle at which the projection data are recorded.

4.2.3 Projection sets

The quantity $\lambda_\phi(x')$ in equation (4.3) may be interpreted as the one-dimensional function λ_ϕ of a single variable x' with ϕ as a parameter, and with the arrangement of figure 4.10 this $\lambda_\phi(x')$ is referred to as a parallel projection. To gather this sort of data, a single source and detector are translated across the object at an angle ϕ_1, producing $\lambda_{\phi_1}(x')$. The gantry is then rotated to ϕ_2 and $\lambda_{\phi_2}(x')$ is obtained, and so on for many other angles. As we mentioned in the previous section, the inefficiencies of this first-generation scanning are no longer tolerated in commercial systems, and the projection data are measured using a fan beam. In this case, the distance x' is measured in a curvilinear fashion around the detector from the centre of the array and ϕ is the angle of the central axis of the projection (see figure 4.11). In what follows we analyse the case for parallel projections simply because it is the easier case to study. The added complexity of fan beam geometry obscures the basic solution method, while adding but little to the intellectual content (see also end of §4.3.1).

In practice, the x-ray source and x-ray detector are of finite size. The projection data are better described as volume integrals over long, thin 'tubes' rather than as line integrals. One effect of this is to average over any detail within the object that is small compared to the lateral dimensions of the tube. The highest spatial frequencies that would be present in a 'perfect' projection are thus not measurable and the object appears to be 'band-limited' because of this low-pass filtering by the measuring system. This has important consequences, which will be discussed later (§4.3).

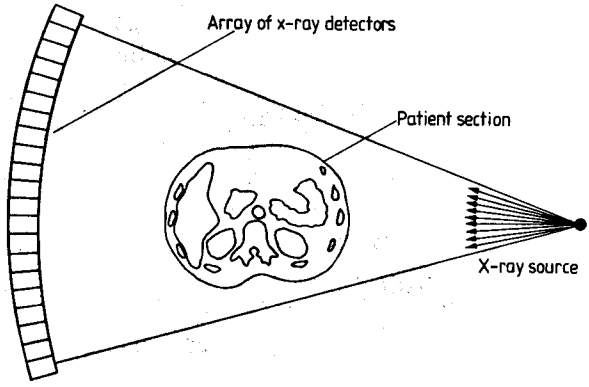

Figure 4.11 For second- and higher-generation systems, data are collected using the fan-beam geometry as shown here.

4.2.4 Information content in projections and the central section theorem

Up to this point, we have assumed that equation (4.3) has a solution. We shall now show that a complete set of projection data do indeed have enough information contained to permit a solution. In doing so, we shall point the way to the method of solution that is most commonly used in x-ray CT scanners.

First we specify the notation. The Fourier transform of the density distribution $\mu[x, y]$ is $M[\zeta, \eta]$. The square brackets serve to remind us that the coordinates are Cartesian. In polar coordinates, the corresponding quantities are $\mu^{\mathrm{P}}(r, \theta)$ and $M^{\mathrm{P}}(\rho, \phi)$. ($M$ is upper-case Greek 'mu'.) The various quantities defined in the $x'y'$ frame are $\mu'[x', y']$, $M'[\zeta', \eta']$, etc. It is not necessary to use the prime on $\lambda_\phi(\ )$, etc, since the different functional form of λ for each ϕ value is implicitly denoted by the subscript ϕ.

The angular orientation of the $[x, y]$ reference frame is arbitrary, so without loss of generality we can discuss the projection at $\phi = 0$. From equation (4.3) we have

$$\lambda_0(x') = \int_{-\infty}^{\infty} \int_{-\infty}^{\infty} \mu[x, y]\delta(x - x')\, \mathrm{d}x\, \mathrm{d}y. \tag{4.4}$$

The integration over x is trivial, i.e.

$$\lambda_0(x) = \int_{-\infty}^{\infty} \mu[x, y]\, \mathrm{d}y \tag{4.5}$$

which is an obvious result anyway.

The next step is to take the one-dimensional Fourier transform of both sides of equation (4.5). Readers unfamiliar with the basic concepts of the Fourier transform may care to study the appendix to Chapter 12 (§12.9) at this point. Writing the transformed quantity as $\Lambda_0(\zeta)$, we have

$$\Lambda_0(\zeta) \equiv \int_{-\infty}^{+\infty} \lambda_0(x) \exp(-2\pi i \zeta x)\, dx$$
$$= \int_{-\infty}^{\infty} \int_{-\infty}^{\infty} \mu[x, y] \exp[-2\pi i(\zeta x + \eta y)]\, dy\, dx \Big|_{\eta=0}. \quad (4.6)$$

An extra term $\exp(-2\pi i \eta y)$ has been slipped into the Fourier kernel on the right-hand side (RHS), but the requirement that the integral be evaluated for $\eta = 0$ makes this a null operation. However, in this form the RHS of equation (4.6) is recognisable as the two-dimensional Fourier transform $M[\zeta, \eta]$ evaluated at $\eta = 0$, so equation (4.6) can be rewritten as

$$\Lambda_0(\zeta) = M[\zeta, 0]. \quad (4.7)$$

Because the Cartesian ζ axis (i.e. $\eta = 0$) coincides with the polar coordinate ρ at the same orientation, equation (4.7) can be written as

$$\Lambda_0(\zeta) = M^{\mathrm{P}}(\rho, 0). \quad (4.8)$$

This is an important result. In words, it says that if we take the one-dimensional Fourier transform of the projection λ_0, the result Λ_0 is also the value of the two-dimensional transform of μ along a particular line. This line is the central section that is oriented along the direction $\phi = 0$. Now we can restore the arbitrary angular origin of the reference frames and state the general result, namely

$$\Lambda_\phi(\zeta') = M'[\zeta', \eta']$$
$$= M^{\mathrm{P}}(\rho, \phi). \quad (4.9)$$

This important result is known as the central section or central slice theorem. To illustrate the theorem, consider a general, bounded object. This object can always be synthesised from a linear superposition of all of its two-dimensional spatial frequency components. Now, consider just one of those cosinusoidal frequency components (see figure 4.12(*a*)). Only when the projection direction is parallel to the wave crests does the projection differ from zero. However, for that particular direction, the full cosine distribution is projected onto the x' axis. The Fourier transform of this one component is shown in figure 4.12(*b*). The original object is a superposition of many component waves of various phases, periods and directions, and it follows that only those waves that are parallel to the first one will have their transforms located on the ξ' axis, and that these are the only waves that will change the form of $\lambda_\phi(x')$. Thus, the transform of the slice is identical to the corresponding section (or slice) of the two-dimensional transform.

4.2.5 Reconstruction by two-dimensional Fourier methods

It now follows that a complete set of projections contains the information that is needed to reconstruct an image of μ. This can be seen by considering a large number of projections at evenly spaced angles ϕ_n.

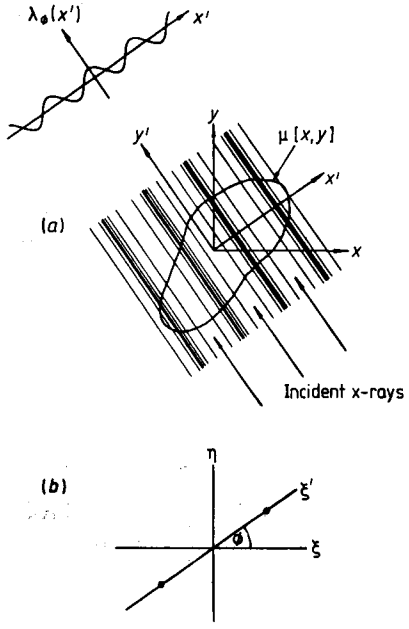

Figure 4.12 (*a*) A general object distribution $\mu(r)$ can be decomposed into Fourier components of the form $\sin(2\pi\rho r)$ or $\cos(2\pi\rho r)$. One of the latter is depicted here. There is only one direction ϕ for which the projection of this component is non-zero, and at this particular ϕ the component is fully mapped onto the projection. (*b*) The Fourier transform of this component is a pair of δ functions (shown here by dots) located on the ξ' axis. (Reproduced from Barrett and Swindell (1981).)

The value of $M^P(\rho, \phi)$ can then be determined along the radial spokes of the same orientations. If M^P is thus defined on a sufficiently well sampled basis (more about this later—§4.5.1), then $\mu[x, y]$ can be obtained by a straightforward two-dimensional transformation of M, which can be obtained from M^P by means of interpolation from the polar to the Cartesian coordinate systems.

It is worth noting that the projections must be taken over a full 180° rotation without any large gap in angle. If there are large gaps, there will be corresponding sectors in Fourier space that will be void of data. The object μ cannot faithfully be constructed from its transform M if this latter is incompletely defined. We shall see in Chapter 6 that certain classes of positron emission tomography scanners suffer the problem of limited-angle projection data.

The solution method just outlined is not a very practicable one for a number of reasons, but the discussion demonstrates that, in principle, an object can be reconstructed from a sufficiently complete set of its projections. The commonly used 'filtered backprojection' method is described in §4.3.

4.2.6 Displaying the image

The reconstruction of μ is usually made on a rectangular array, where each element or pixel has a value μ_i ascribed to it ($1 \leqslant i \leqslant I$). Before these data are displayed on a video screen, it is conventional to rescale them in terms of a 'CT number', which is defined as

$$\text{CT number} = \frac{\mu_{\text{tissue}} - \mu_{\text{water}}}{\mu_{\text{water}}} \times 1000. \tag{4.10}$$

Thus the CT number of any particular tissue is the fractional difference of its linear attenuation coefficient relative to water, measured in units of 0.001, i.e. tenths of a per cent. The CT numbers of different soft tissues are relatively close to each other and relatively close to zero. However, provided that the projection data are recorded with sufficient accuracy, then different soft tissues can be differentiated with a high degree of statistical confidence. Similar tissues, which could not be resolved on conventional transmission x-radiographs, can be seen on CT reconstructions. Small differences in CT number can be amplified visually by increasing the contrast of the display. The output brightness on the screen is related to the CT number by means of a level and a width control (see figure 4.13). These windowing controls can be varied by the operator while looking at the image, so the small range of CT numbers corresponding to the soft tissues within the body can be selected to drive the screen from black to white.

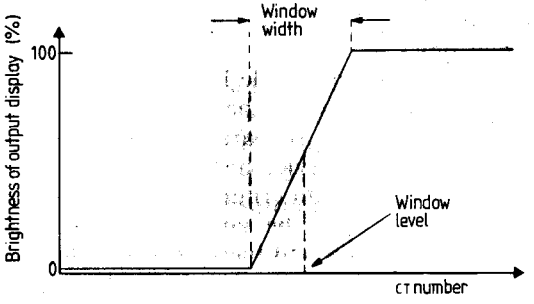

Figure 4.13 The 'windowing' facility allows the display brightness range to be fully modulated by any desired range of CT values as determined by adjusting the window 'level' and 'width'.

4.3 FOURIER-BASED SOLUTIONS: THE METHOD OF CONVOLUTION AND BACKPROJECTION

The mathematics of transmission computed tomography, or the theory of reconstruction from projections, has itself acquired the status of attracting attention as an independent research area. The literature is

enormous and there already exist many excellent books reviewing the field. Some, such as Herman (1980), review the subject from the viewpoint of the theoretically minded physicist or engineer, whereas others, for example Natterer (1986), are really only accessible to persons who first and foremost regard themselves as mathematicians. Optionally, for a practical discussion, the book by Barrett and Swindell (1981) may be consulted. Against the backcloth of this formidable weight of literature, the purpose of this chapter is to provide a simplified view of theory applicable to the most elementary scanning geometry in order to come to grips with some basic principles. From this beginning, it should be possible to go on to view the analogous developments in single-photon emission computed tomography (Chapter 6) as well as reconstruction techniques using ultrasound (Chapter 7) and nuclear magnetic resonance (Chapter 8). The serious research student will find the treatment in this chapter over-simple and could do no better than branch out starting with one of the above books.

The theory of reconstruction from projections pre-dates the construction of any practical scanner for computed tomography. It is generally accepted that the problem was first analysed by Radon (1917) some 70 years or so ago. The theory has been 'rediscovered' in several distinct fields of physics including radioastronomy (Bracewell and Riddle 1967) and electron microscopy (Gilbert 1972). An account of a method and the first system for reconstructing x-ray medical images probably originated from Russia (Tetel'baum 1956, 1957, Korenblyum *et al* 1958) (see Chapter 1), although it is the work of Hounsfield (1973) that led to the first commercially developed system. This was a head scanner marketed by EMI. Many different techniques for solving the reconstruction problem have been devised and, in turn, each of these has received a great deal of attention regarding subtle but important additional features that improve image quality. It would be true to say that, just as scanner hardware has developed rapidly, so parallel developments in reconstruction theory have kept pace to service new designs and to predict optimal scanning conditions and the design criteria for new scanners.

Reconstruction techniques can be largely classified into two distinct groups, namely the convolution and backprojection methods (or equivalent Fourier techniques) and iterative methods. For a long time, there was much debate as to the relative superiority of one algorithm or another, and, in particular, whether one of the two classes was in some way superior. Today, this debate has largely subsided, with the inevitable conclusion that each method has its advantages, it being important to tailor the reconstruction technique to the scanner design and (in a wider context) to the physics of the imaging modality. For example, iterative techniques have found some important applications in emission CT where photon statistics are poorer.

Next we derive the algorithm that is most commonly used in CT scanners. It is the method of 'filtered backprojection' or 'convolution and backprojection'. A formal statement of the two-dimensional inverse polar Fourier transform yielding $\mu[x, y]$ is given by

$$\mu^{\mathrm{P}}(r, \theta) = \mu[x, y]$$

$$= \int_0^{\pi} \int_{-\infty}^{\infty} M^{\mathrm{P}}(\rho, \phi) \exp[2\pi i\rho(x \cos\phi + y \sin\phi)]|\rho| \, \mathrm{d}\rho \, \mathrm{d}\phi \quad (4.11)$$

where $x(= r\cos\theta)$ and $y(= r\sin\theta)$ denote the general object point.

If equation (4.11) is broken into two parts, the method of solution becomes immediately apparent (indeed, these two equations give the method its name):

$$\mu[x, y] = \int_0^{\pi} \lambda^{\dagger}_{\phi}(x') \, \mathrm{d}\phi \Big|_{x'=x\cos\phi+y\sin\phi} \quad (4.12)$$

where

$$\lambda^{\dagger}_{\phi}(x') = \int_{-\infty}^{\infty} M^{\mathrm{P}}(\rho, \phi)|\rho|\exp(2\pi i\rho x') \, \mathrm{d}\rho. \quad (4.13)$$

Consider equation (4.13), which defines an intermediate quantity $\lambda^{\dagger}$. For reasons that will become obvious, $\lambda^{\dagger}$ is called the filtered projection. The first point to notice is that equation (4.13) is the one-dimensional Fourier transform of the product of M^{P} and $|\rho|$. As such, it should also be possible to write it as the convolution of the Fourier transforms of M^{P} and $|\rho|$ (see the appendix of Chapter 12, §12.9.2). Taking M^{P} first, its transform is known from the central slice theorem. It is just the projection data, $\lambda_{\phi}(x')$, i.e.

$$\lambda_{\phi}(x') = \int_{-\infty}^{\infty} \Lambda_{\phi}(\zeta') \exp(2\pi i\zeta' x') \, \mathrm{d}\zeta' \quad (4.14)$$

where, from (4.9),

$$\Lambda_{\phi}(\zeta') = M^{\mathrm{P}}(\rho, \phi).$$

Now consider $|\rho|$. This is not a sufficiently well behaved function for its transform to exist. In practice, however, we have seen in §4.2.3 that $M(\rho, \phi)$ is band-limited by the measuring system, so if the maximum frequency component of $M(\rho, \phi)$ is $\rho_{\max}$ then $|\rho|$ can be similarly truncated. Thus we need the transform $p(x')$ of $P(\rho)$, where

$$\begin{aligned} P(\rho) &= 0 \qquad & |\rho| \geqslant \rho_{\max} \\ P(\rho) &= |\rho| \qquad & |\rho| < \rho_{\max} \end{aligned} \quad (4.15)$$

i.e.

$$p(x') = \int_0^{\rho_{\max}} \rho \exp(2\pi i\rho x') \, \mathrm{d}\rho - \int_{-\rho_{\max}}^{0} \rho \exp(2\pi i\rho x') \, \mathrm{d}\rho. \quad (4.16)$$

Equation (4.16) is straightforward to evaluate (see appendix, §4.6), with the result

$$p(x') = \rho^2_{\max}[2\,\mathrm{sinc}(2\rho_{\max}x') - \mathrm{sinc}^2(\rho_{\max}x')] \quad (4.17)$$

which is perfectly well behaved.

Using the convolution theorem, equation (4.13) can now be written as

$$\lambda^{\dagger}_{\phi}(x') = \int_{-\infty}^{\infty} \lambda_{\phi}(x)p(x' - x) \, \mathrm{d}x \quad (4.18)$$

or in the conventional shorthand notation (* denoting convolution)

$$\lambda^{\dagger}_{\phi}(x') = \lambda_{\phi}(x') * p(x'). \tag{4.19}$$

The dagger (†) indicates a *filtered* projection because the original projection is convolved with $p(x')$, which constitutes a filtering operation.

Now we look at equation (4.12). This represents the process of *backprojection* in which a given filtered projection $\lambda^{\dagger}_{\phi}$ is distributed over the $[x, y]$ space. For any point x, y and projection angle ϕ, there is a value for x' given by

$$x' = x\cos\phi + y\sin\phi.$$

This is the equation of a straight line (parallel to the y' axis), so the resulting distribution has no variation along the y' direction. A simple analogy is to think of dragging a rake, with a tooth profile given by $\lambda^{\dagger}_{\phi}(x')$, though gravel in the y' direction. The one-dimensional tooth profile is transferred to the two-dimensional bed of gravel. Backprojection is not the inverse of projection. If it were, the reconstruction-from-projection problem would be trivial! It is very important to be clear that pure backprojection of unfiltered projections will not suffice as a reconstruction technique. Equation (4.12) also contains an integration over ϕ, which represents the summation of the backprojections of each filtered projection, each along its own particular direction. It is like raking the gravel from each projection direction with a different tooth profile for each filtered projection. The analogy breaks down, however, since each raking operation would destroy the previous distribution rather than adding to it, as required by the integration process.

The total solution is now expressed by equation (4.19) and equation (4.12). In words, each projection $\lambda_{\phi}(x')$ is convolved (filtered) with $p(x')$ (equation (4.17)). The filtered projections are each backprojected into $[x, y]$ and the individual backprojections (for each projection angle) are summed to create the image $\mu[x, y]$.

4.3.1 A practical implementation

In practice, the data are discretely sampled values of $\lambda_{\phi}(x')$. Thus the continuous convolution of equation (4.18) must be replaced by a discrete summation, as must also the angular integration of equation (4.12). We deal first with the convolution. The Whittaker–Shannon sampling theorem states that a band-limited function with maximum frequency component $\rho_{\max}$ can be completely represented by, and reconstructed from, a set of uniform samples spaced s apart, where $s \leqslant (2\rho_{\max})^{-1}$. This requirement corresponds to adjacent samples being taken approximately $w/2$ apart, where w is the width of a detector. Provided that the data are band-limited in this manner, the continuous convolution can be replaced by a discrete convolution. Grossly mislead-

ing results can occur if the sampling is too wide to satisfy this Nyquist condition.

From equation (4.17) and using $s = (2\rho_{max})^{-1}$, it is seen that

$$\begin{aligned} p(ms) &= 0 && m \text{ even}, m \neq 0 \\ p(ms) &= -(\pi ms)^{-2} && m \text{ odd} \\ p(ms) &= (2s)^{-2} && m = 0 \end{aligned} \tag{4.20}$$

where ms denotes the positions along x' at which the discrete filter is defined. The projection data λ_ϕ are sampled at the same intervals, so that equation (4.18) can be replaced by its discrete counterpart

$$\lambda^{\dagger}_{\phi}(ms) = \frac{1}{4s}\lambda_\phi(ms) - \frac{1}{\pi^2 s}\sum_{(m-n)\text{odd}}^{n}\frac{\lambda_\phi((m-n)s)}{(m-n)^2} \tag{4.21}$$

where m and n are integers. Figure 4.14 shows the continuous and sampled versions of $p(x')$.

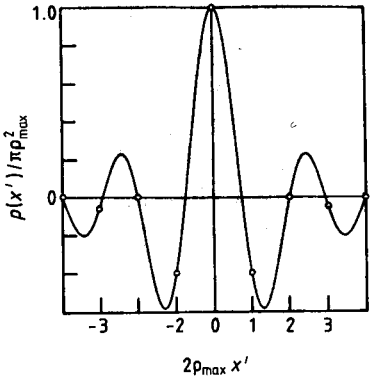

Figure 4.14 The full curve shows continuous form of the Ramachandran–Lakshminarayanan filter. The open circles show the points at which the filter is sampled for digital filtering methods. (Reproduced from Barrett and Swindell (1981).)

Equation (4.21) is the result obtained in a quite different way in the classic paper by Ramachandran and Lakshminarayanan (1971) and is the discrete version of the result obtained by Bracewell and Riddle (1967). Note that, although the Fourier transform has featured in its derivation, the reconstruction technique is entirely a real-space operation. The convolution function (the transform of the bounded $|\rho|$) is the same for all the projections and can therefore be computed, stored and re-used for each projection. Equations (4.12) and (4.21) show that the contributions to the reconstruction $\mu[x, y]$ can be computed from the projections

one by one, as they arrive from the scanner, and once 'used' the projection may be discarded from computer memory. This is a distinct advantage over the two-dimensional Fourier transform method (§4.2.5) of recovering $\mu[x, y]$, when all the transformed projections are in use simultaneously. One can even view the reconstruction 'taking shape' as the number of contributing projections increases.

The discrete backprojection is shown in figure 4.15. It is necessary to assign and then sum to each element in the image array μ_i the appropriate value of $\lambda^{\dagger}_{\phi}$. This can be done on a nearest-neighbour basis, but it is better to interpolate between the two nearest sampled values of $\lambda^{\dagger}_{\phi}$. Formally, the process is described by

$$\mu_i = \sum_{n=1}^{N} \lambda^{\dagger}_{\phi_n}(m^* s) \tag{4.22}$$

where subscript n denotes the nth projection and m^* denotes an interpolated point within m for which the interpolated value of $\lambda^{\dagger}$ is calculated. The backprojection through m^* passes through the centre of the ith pixel.

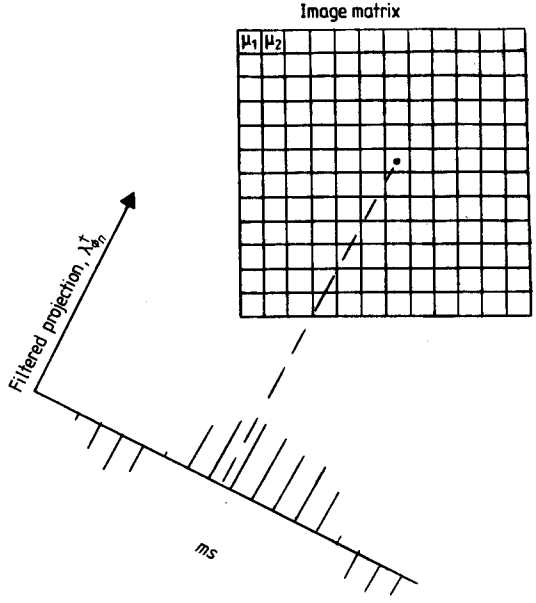

Figure 4.15 The object is reconstructed into an array of pixels μ_1, μ_2, . . . by backprojecting each filtered projection onto the array and summing the results for each projection angle.

The total process is not so daunting as it seems. For parallel projection data, the whole process can be coded into less than 25 lines of FORTRAN code (see figure 4.16).

```
      DIMENSION P(65),PSTAR(65),F(4225)
      DATA W/.3333333/, M/50/, F/4225*0./
C  FOLLOWING STEPS ARE DONE FOR EACH PROJECTION
      DO 50 K=1,M
C READ ONE SET PROJECTION DATA AND ANGLE
      READ (1,100) P,PHI
100   FORMAT (66F6.2)
      SINE = SIN(PHI)
      COSINE = COS(PHI)
C CALCULATE FILTERED PROJECTION PSTAR
      DO 30 I=1,65
      Q = P(I)*2.467401
      JC = 1 + MOD(I,2)
      DO 20 J=JC,65,2
20    Q = Q - P(J)/(I-J)**2
30    PSTAR(I) = Q/(3.141593*M*W)
C BACK PROJECT FILTERED PROJECTION ONTO IMAGE ARRAY
      DO 50 J=1,65
      IMIN = J*65-32-INT(SQRT(1024.-(33-J)**2)
      IMAX = (2*J-1)*65 - IMIN + 1
      X = 33 + (33-J)*SINE + (IMIN-J*65+31)*COSINE
      DO 50 I=IMIN,IMAX
      X = X + COSINE
      IX = X
50    F(I) = F(I) + PSTAR(IX) + (X-IX)*(PSTAR(IX+1)-PSTAR(IX))
C DENSITY VALUES ARE NOW STORED IN F ARRAY READY FOR PRINTOUT
      STOP
      END
```

Figure 4.16 Despite the apparent complexity, the reconstruction process of filtering the projections and backprojecting into the image array can be coded into just a few lines of FORTRAN. This code is for parallel-beam reconstruction. (After Brooks and Di Chiro (1975).)

Returning briefly to the filtering operation, it is sometimes advantageous to reduce the emphasis given to the higher-frequency components in the image for the purpose of reducing the effects of noise. One widely used filter due to Shepp and Logan (1974) replaces $|\rho|$ with

$$|(2\rho_{\max}/\pi)\sin(\pi\rho/2\rho_{\max})|$$

(see figure 4.17). The digital filter has the form

$$p(ms) = -2(\pi s)^{-2}(4m^2 - 1)^{-1} \qquad m = 0, \pm 1, \pm 2, \ldots . \quad (4.23)$$

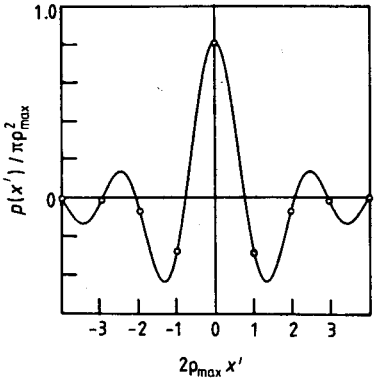

Figure 4.17 The continuous and discrete versions (full curve and open circles, respectively) of the Shepp and Logan filter. (Reproduced from Barrett and Swindell (1981).)

Another widely used filter, the Hanning window, uses an apodising factor $A(\rho)$ given by

$$A(\rho) = \alpha + (1 - \alpha)\cos(\pi\rho/\rho_{\max})$$

which multiplies into $|\rho|$. The quantity α is a variable parameter that gives $A(0) = 1$ for all α and $A(\rho_{\max}) = 2\alpha - 1$ varying from -1 for $\alpha = 0$ to 1 for $\alpha = 1$. In practical terms, when $A(\rho)$ is included on the RHS of equation (4.13), this becomes equivalent to convolving the projection data $\lambda_\phi(x')$ with a modified kernel $p(x')$ whose form is different from that in equation (4.17) (or discretely, equation (4.20)). A fuller discussion of windowing is given in the section on single-photon emission computed tomography (§6.7).

In this section, the filtered backprojection method has been described. Since both the filtering and the backprojection are linear and shift-invariant operations, it does not matter which is performed first. When backprojection is performed first, however, the filtering becomes a two-dimensional operation. Backprojecting unfiltered projections would yield a result $\mu_B[x, y]$, where

$$\mu_B[x, y] = \int_0^\pi \lambda_\phi(x')\, d\phi \Big|_{x'=x\cos\phi+y\sin\phi}. \tag{4.24}$$

Rewriting equation (4.14) for the central slice theorem, we have

$$\lambda_\phi(x') = \int_{-\infty}^{\infty} \left(\frac{M^P(\rho, \phi)}{|\rho|}\right) |\rho| \exp(2\pi i\rho x')\, d\rho. \tag{4.25}$$

Comparing the pairs of equations (4.24) and (4.25) with (4.12) and (4.13), it is quite clear that $\mu_B[x, y]$ is related to $\mu[x, y]$ by a function that compensates for the denominator in the integral (4.25). Deconvolution of this function from $\mu_B[x, y]$ to yield $\mu[x, y]$ is possible, but is a very clumsy way of tackling the reconstruction problem. If it is also remembered that filtering can take place in real space (by convolution) or Fourier space, it is clear that there are many equivalent ways of actually performing the reconstruction process (Barrett and Swindell 1981).

After the first generation of transmission CT scanners, the technique of rotate–translate scanning was largely abandoned in favour of faster scanning techniques involving fan-beam geometry. Viewed at the primitive level, however, these scanning geometries merely in-fill Fourier space in different ways and a reconstruction of some kind will always result. Indeed, it is perfectly possible to imagine merging projection data for the same object taken in quite different geometries. Once this is realised, it is soon apparent that the multitude of reconstruction methods that exist are in a sense mere conveniences for coping with less-simple geometry. The methods do, however, possess some elegance and many of the derivations are quite tricky! Without wishing to be overdismissive of a very important practical subject, we shall make no further mention of the mathematics of more complex geometries for reconstructing two-dimensional tomograms from one-dimensional

projections. Similar reconstruction techniques have been used for x-ray transmission cone-beam tomography, whereby the x-rays are collimated to a cone and impinge on an *area* detector (see e.g. Feldkamp *et al* 1984, Webb *et al* 1987). There are also other quite ingenious methods for obtaining transmission tomograms that rely on very different mathematics: for example, circular tomography (Smith and Kruger 1987), whereby every point within the patient is projected onto a circle on the face of an image intensifier by the circular motion of the focal spot of a custom-designed x-ray tube. Selected planes are brought into focus by optically tracking an annular viewing field across the image intensifier with the diameter of the annulus defining the plane of interest. Circular tomography is somewhat intermediate between classical tomography, which requires no reconstruction mathematics, and x-ray CT, since circular tomography demands that the recorded data be decoded before they are able to be interpreted.

4.4 ITERATIVE METHODS OF RECONSTRUCTION

In the early days of computed tomography, iterative methods were popular. Various techniques with names such as ART (algebraic reconstruction technique), SIRT (simultaneous iterative reconstruction technique) and ILST (iterative reconstruction technique) were proposed and implemented. Such methods are no longer used for x-ray CT but still find application where the data sets are very noisy or incomplete, as they often are in emission computed tomography (see Chapter 6).

The principle of the method is described in figure 4.18. The image (the estimate of the object) is composed of I two-dimensional square pixels with densities μ_i, $1 \leqslant i \leqslant I$. The projections $\hat{\lambda}(\phi, x')$ that would occur if this were the real object are readily calculated using

$$\hat{\lambda}(\phi, x') = \sum_{i=1}^{I} \alpha_i(\phi, x')\mu_i \tag{4.26}$$

where $\alpha_i(\phi, x')$ is the average path length traversed by the (ϕ, x') projections through the ith cell. These coefficients need only be calculated once; they can then be stored for future use. For a typical data set, equation (4.26) represents 10^5 simultaneous equations. The solution method is to adjust the values of the μ_i iteratively until the computed projections $\hat{\lambda}$ most closely resemble the measured projections λ. These final values μ_i are then taken to be the solution, i.e. the image. Equation (4.26) is not soluble using direct matrix inversion for a variety of reasons that relate not only to the size (α is typically a $10^5 \times 10^5$ square matrix, albeit a very sparse one) but also to the conditioning of the data.

Because of measurement noise, and the approximations engendered by the model, there will not be a single exact solution. The arguments are very similar to those in Chapter 12 explaining why image deconvolution is difficult. Furthermore, there are usually far more equations than

there are unknowns, so a multiplicity of solutions may exist. Part of the difficulty of implementing the solution is in deciding upon the correct criteria for testing the convergence of the intermediate steps and knowing when to stop. This is but one example of a whole class of *ill-posed* problems, which in recent years has necessitated the development of a new branch of mathematics bearing this same name.

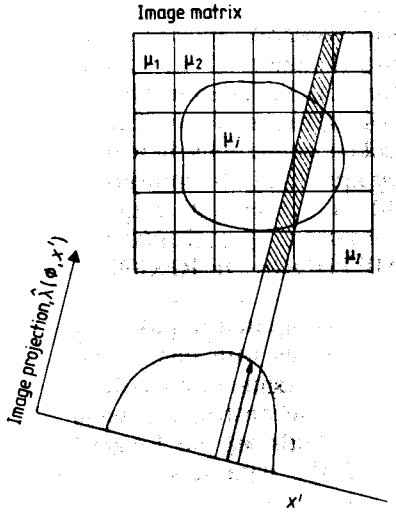

Figure 4.18 In iterative reconstruction methods, a matrix of I cells represents the object. The line integrals for the projection data are then replaced by a set of linear equations (4.26). (Reproduced from Barrett and Swindell 1981)

The many iterative algorithms differ in the manner in which the corrections are calculated and reapplied during each iteration. They may be applied additively or multiplicatively; they may be applied immediately after being calculated; optionally, they may be stored and applied only at the end of each round of iteration. The order in which the projection data are taken into consideration may differ as well.

The simple example shown in figure 4.19 illustrates additive immediate correction. Four three-point projections are taken through a nine-point object O, giving rise to projection data sets P_1 through P_4. Taken in order, these are used successively to calculate estimates E_1 through E_4 of the original object.

The initial estimate is obtained by allocating, with equal likelihood, the projection data P_1 into the rows of E_1. Subsequent corrections are made by calculating the difference between the projection of the previous estimate and the true projection data and equally distributing the difference over the elements in the appropriate row of the new

estimate. For example, the difference between the projection of the first column of E_1 shown in parentheses (15), and the true measured value (16) is 1. In creating the first column of E_2, one-third of this difference ($\frac{1}{3}$) is added to each element of the first column of E_1. The first iteration is completed with the calculation of E_4. That the process converges in this numerical example is demonstrated by calculating the root-mean-square (RMS) deviation of elements of E_1 through E_4 from the true values in O. As the figure shows, these RMS errors decrease monotonically.

Further discussion of iterative algorithms is detailed in the book by Herman (1980) and the review article by Webb (1981).

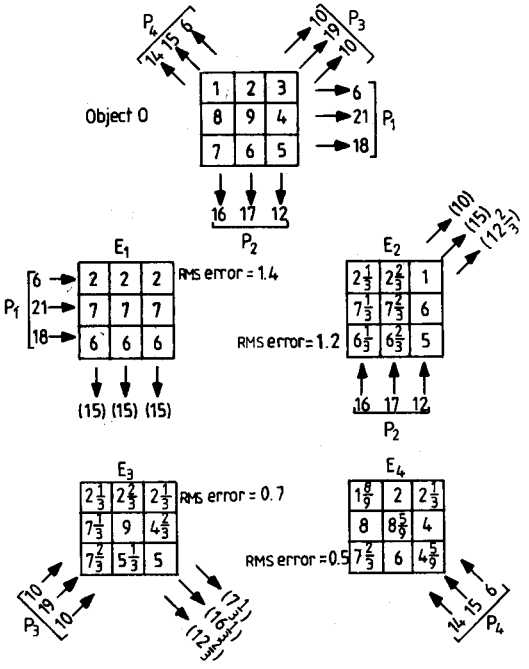

Figure 4.19 A simple example of iterative reconstruction. See text for explanation.

4.5 OTHER CONSIDERATIONS

4.5.1 Angular-sampling requirements

Assuming a point-like source of x-rays, the effect of having a rectangular detector profile of width w in the direction of the projection is to modulate the spectrum of the projection with a $\sin(\pi\rho w)/\pi\rho w$ apodisation. The first zero of this function is at $\rho = 1/w$. If we equate this to

the maximum frequency component, i.e. $\rho_{max} = 1/w$, then the sampling interval s along the projection must be $s \leq w/2$, as required by the sampling theorem (see also §12.6). Frequencies higher than ρ_{max} will, of course, persist in the sidelobes of the apodising function but at greatly reduced amplitudes, so the sampling requirement is only approximately fulfilled. Additional high-frequency attenuation will take place, however, owing to the finite source size (and possibly patient motion), and this $w/2$ criterion is found to be an acceptable compromise between generating aliasing artefacts and processing massive amounts of data. The question regarding the number N_ϕ of angular samples remains. The number N_ϕ is taken to be the number of projections in the range $0 \leq \phi < 180°$.

If the final image is to have equal resolution in all directions, then the highest spatial-frequency components must be equally sampled in the radial and azimuthal directions in the neighbourhood of $\rho = \rho_{max}$ in the (ρ, ϕ) Fourier space.

For an object space of diameter D and projection data that are sampled with an interval d, the number of samples per projection is $N_s = D/d$ and the radial sampling interval in Fourier space is thus $2\rho_{max}d/D$. The azimuthal interval at $\rho = \rho_{max}$ is $\rho_{max}\Delta\phi$, where $\Delta\phi = \pi/N_\phi$. Equating these sampling intervals yields the result

$$N_\phi = (\pi/2)N_s. \tag{4.27}$$

In practice, projections are usually taken over 360° to reduce partial-volume and other artefacts, so $2N_\phi$ projections are usually taken. Equivalently, the angular increment in projection angle is

$$\Delta\phi = 2/N_s \tag{4.28}$$

for a uniformly sampled image data set.

4.5.2 Dose considerations

The projection data are subject to measurement noise. If a particular measurement were repeated many times, yielding an average measured value of n detected x-ray photons, then the random noise associated with a single reading will be $\sqrt{n}$. These fluctuations result from the Poisson statistics of the photon beam, and cannot be eliminated. These measurement fluctuations propagate through the reconstruction algorithms, with the result that a perfectly uniform object of density μ will appear to have a mottled appearance. A signal-to-noise ratio (SNR) can be defined as

$$\text{SNR} = \mu/\Delta\mu \tag{4.29}$$

where $\Delta\mu$ is the RMS fluctuation in the reconstructed value of μ about its mean value.

On the assumption that this photon noise is the only source of noise in the image, several authors (see for example Barrett *et al* 1976) have determined an expression relating the x-ray dose U delivered to the centre of a cylindrical object to the spatial resolution ε and the

signal-to-noise ratio SNR. The expression has the form

$$\eta U = k_1(\text{SNR})^2/\varepsilon^3 b \tag{4.30}$$

where b is the thickness of the slice, η is the detective quantum efficiency of the detector, and k_1 is a constant that depends on beam energy, the diameter of the object and the precise manner in which ε is defined. The points to note are that the dose depends on the second power of the signal-to-noise ratio and, to all intents and purposes, on the inverse fourth power of the resolution. This latter claim is made because in any reasonable system the slice width will be scaled in proportion to the resolution required: thickness $b = k_2\varepsilon$ where k_2 is typically 2–5, i.e. the reconstruction voxel is a rather skinny, rectangular, parallelepiped. If k_2 becomes too large, partial-volume effects, as described in the next section, will become obtrusive.

Figure 4.20 shows how the quantities are related for a typical beam energy and object size. It is seen that dose levels in the range of 0.01 to 0.1 Gy are delivered to produce images with millimetre resolution at approximately 1% density discrimination. These are the dose levels that are actually found in practice, and one therefore presumes that commercial CT scanners are operating at, or close to, this photon-limited situation. The 16-fold increase in dose that would be needed for even a modest two-fold increase in resolution would seem to negate the possibility of improving the spatial resolution. Fortuitously, submillimetre resolution of bony structures can be obtained without invoking these unacceptably high dose levels. This is because the bone/tissue interface has a density ratio of almost 2:1 and the SNR can be traded off to improve the spatial resolution without escalating the dose. Of course, it requires finer sampling of the projection data. A new research tool has recently been announced—Superscope (Flannery *et al* 1987a,b) to perform tomographic microscopy with a resolution 1000 times that of medical x-ray CT. In view of the dose–resolution constraint expressed by equation (4.30), the enormous intensity of the Brookhaven National

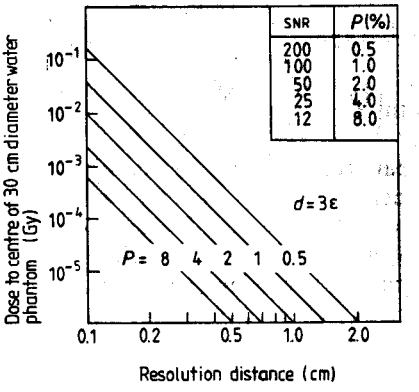

Figure 4.20 Nomogram relating dose U, density discrimination (SNR) and resolution ε for a typical diagnostic CT scanner.

Laboratory synchrotron source was harnessed. The instrument has been used to visualise the internal structure of insects.

4.5.3 Partial-volume artefacts

Because the x-ray beam diverges in a direction perpendicular to the slice, a projection measured in one direction may be slightly different from the projection taken along the same path but in the opposite direction. This provides one reason for requiring a full 360° scan of the patient. The inconsistencies in the data can be compensated by combining data from opposite directions.

A different but related partial-volume effect arises from the observation that the anatomical structures do not in general intersect the section at right angles. A long, thin voxel could well have one end in soft tissue and the other end in bone. As a result the reconstructed μ would have an intermediate value that did not correspond to any real tissue at all. This is the main reason for scaling d with ε and not letting k_2 get too large (see previous section).

4.5.4 Beam-hardening artefacts

As the x-ray beam passes through tissue, the lower-energy components are attenuated more rapidly than the higher-energy components. The average photon energy increases; the beam becomes *harder*. As a result, the exponential law of attenuation no longer holds.

With no absorber in the beam, the detector output is

$$I_0 = k_3 \int_0^{E_{\max}} S(E)\, \mathrm{d}E \tag{4.31}$$

where the source spectrum $S(E)$ is defined such that $S(E)\,\mathrm{d}E$ is the energy fluence in the energy range E to $E + \mathrm{d}E$.

With an object in the beam, Beer's law must be weighted by the energy spectrum and integrated, to give

$$I = k_3 \int_0^{E_{\max}} S(E) \exp\left(- \int_{\mathrm{AB}} \mu_{\mathrm{E}}[x, y]\, \mathrm{d}y'\right) \mathrm{d}E \tag{4.32}$$

and the projection λ is thus

$$\lambda = - \ln\left(\frac{\int_0^{E_{\max}} S(E) \exp(- \int_{\mathrm{AB}} \mu_{\mathrm{E}}[x, y]\, \mathrm{d}y')\, \mathrm{d}E}{\int_0^{E_{\max}} S(E)\, \mathrm{d}E}\right). \tag{4.33}$$

It is this *non*-linear relationship between λ and μ that causes the problem. The principal effects of this artefact show up as a false reduction in density in the centre of a uniform object and the creation of false detail in the neighbourhood of bone/soft tissue interfaces. These artefacts are particularly troublesome in the skull. There are several ways that the problems can be overcome, and at this point the reader is referred to the appropriate literature.

We thus complete our, albeit brief, presentation of the important concepts of x-ray CT. The reconstruction theory itself has a certain

elegant simplicity using simple assumptions concerning the physics of the data assembly. We have seen how imaging hardware is constructed to realise the theory and how in a relatively brief timespan this equipment has been optimised. In the next chapter we shall complement this discussion by describing how, in addition to its role as a diagnostic device, the CT scanner has found a fundamental place in aiding the planning of radiotherapy treatment.

4.6 APPENDIX

4.6.1 Evaluation of the Fourier transform p(x') of the band-limited function $|\rho|$

We start from equation (4.16), which is integrated as follows:

$$p(x') = \int_0^{\rho_{max}} \rho \exp(2\pi i \rho x')\, d\rho - \int_{-\rho_{max}}^{0} \rho \exp(2\pi i \rho x')\, d\rho$$

$$= \left[\frac{\rho \exp(2\pi i \rho x')}{2\pi i x'}\right]_0^{\rho_{max}} - \int_0^{\rho_{max}} \frac{\exp(2\pi i \rho x')\, d\rho'}{2\pi i x'}$$

$$- \left[\frac{\rho \exp(2\pi i \rho x')}{2\pi i x'}\right]_{-\rho_{max}}^{0} + \int_{-\rho_{max}}^{0} \frac{\exp(2\pi i \rho x')\, d\rho'}{2\pi i x'}$$

$$= \frac{\rho_{max} \sin(2\pi \rho_{max} x')}{\pi x'} - \left[\frac{\exp(2\pi i \rho x')}{(2\pi i x')^2}\right]_0^{\rho_{max}} + \left[\frac{\exp(2\pi i \rho x')}{(2\pi i x')^2}\right]_{-\rho_{max}}^{0}$$

$$= 2\rho_{max}^2 \operatorname{sinc}(2\rho_{max} x') + \frac{\cos(2\pi \rho_{max} x') - 1}{2\pi^2 x'^2}$$

$$= 2\rho_{max}^2 \operatorname{sinc}(2\rho_{max} x') - \rho_{max}^2 \operatorname{sinc}^2(\rho_{max} x').$$

We thus obtain the result given by equation (4.17), i.e.

$$p(x') = \rho_{max}^2 [2 \operatorname{sinc}(2\rho_{max} x') - \operatorname{sinc}^2(\rho_{max} x')].$$

REFERENCES

BARRETT H H, GORDON S K and HERSHEL R S 1976 Statistical limitations in transaxial tomography *Comput. Biol. Med.* **6** 307

BARRETT H H and SWINDELL W 1981 *Radiological Imaging: The Theory of Image Formation, Detection and Processing* vol II (New York: Academic Press) p384

BRACEWELL R N and RIDDLE A C 1967 Inversion of fan-beam scans in radio astronomy *Astrophys. J.* **150** 427–34

BROOKS R A and DI CHIRO G 1975 Theory of image reconstruction in computed tomography *Radiology* **117** 561–72

—— 1976 Principles of computer assisted tomography (CAT) in radiographic and radioisotope imaging *Phys. Med. Biol.* **21** (5) 689–732

COULAM C M, ERICKSON J J and GIBBS S J 1981 Image and equipment considerations in conventional tomography *The Physical Basis of Medical Imaging* ed C M Coulam, J J Erickson, F D Rollo and A E James (New York: Appleton-Century-Crofts)

FELDKAMP L A, DAVIS L C and KRESS J W 1984 Practical cone-beam tomography *J. Opt. Sci. Am.* A **1** (6) 612–19

FLANNERY B P, DECKMAN H W, ROBERGE W G and D'AMICO K L 1987a Superscope *Sci. Am.* July pp21–2

—— 1987b Three dimensional X-ray microtomography *Science* **237** 1439–44

GILBERT P 1972 Iterative methods for the three-dimensional reconstruction of an object from projections *J. Theor. Biol.* **36** 105–17

HERMAN G T 1980 *Image Reconstruction from Projections: The Fundamentals of Computed Tomography* (New York: Academic Press)

HOUNSFIELD G N 1973 Computerised transverse axial scanning (tomography). Part 1: Description of system *Br. J. Radiol.* **46** 1016–22

KAK C K 1979 Computerised tomography with x-ray, emission and ultrasound sources *Proc. IEEE* **67** (9) 1245–72

KORENBLYUM B I, TETEL'BAUM S I and TYUTIN A A 1958 About one scheme of tomography *Bull. Inst. Higher Educ. – Radiophys.* **1** 151–7 (translated from the Russian by H H Barrett, University of Arizona, Tucson)

MACDONALD J S 1981 Computed tomography in a clinical setting *Computerized Axial Tomography in Oncology* ed J E Husband and P A Hobday (Edinburgh: Churchill Livingstone) p5

MARAVILLA K R and PASTEL M S 1978 Technical aspects of CT scanning *Comput. Tomogr.* **2** 137–44

NATTERER S 1986 *The Mathematics of Computerised Tomography* (New York: Wiley)

PARKER R P, CONTIER DE FREITAS L, CASSELL K J, WEBB S and HOBDAY P A 1980 A method of implementing inhomogeneity corrections in radiotherapy treatment planning *J. Eur. Radiother.* **1** (2) 93–100

PESCHMANN K R, NAPEL S, COUCH J L, RAND R E, ALEI R, ACKELSBERG S M, GOULD R and BOYD D P 1985 High speed computer tomography: systems and performance *Appl. Opt.* **24** 4052–60

RADON J 1917 Uber die Bestimmung von Funktionen durch ihre Integralwerte langs gewisser Mannigfaltigkeiten *Ber. Verh. Sachs. Akad. Wiss. Leipzig Math. Phys. Kl.* **69** 262–77

RAMACHANDRAN G N and LAKSHMINARAYANAN A V 1971 Three-dimensional reconstruction from radiographs and electron micrographs: applications of convolutions instead of Fourier transforms *Proc. Natl Acad. Sci. USA* **68** 2236–40

SHEPP L A and LOGAN B F 1974 The Fourier reconstruction of a head section *IEEE Trans. Nucl. Sci.* **NS-21** 21–43

SMITH S W and KRUGER R A 1987 Fast circular tomography device for cardiac imaging: image deflection mechanism and evaluation *IEEE Trans. Med. Imaging* **MI-6** (2) 169–73

TETEL'BAUM S I 1956 About the problem of improvement of images obtained with the help of optical and analog instruments *Bull. Kiev Polytechnic Inst.* **21** 222

—— 1957 About a method of obtaining volume images with the help of x-rays *Bull. Kiev Polytechnic Inst.* **22** 154–60 (translated from the Russian by J W Boag, Institute of Cancer Research, London)

WEBB S 1981 Reconstruction of cross-sections from transmission projections: a short simplified review and comparison of performance of algorithms *Physical Aspects of Medical Imaging* ed M Moores, R P Parker and B Pullan (New York: Wiley)

—— 1987 A review of physical aspects of x-ray transmission computed tomography *IEE Proc.* A **134** (2) 126–35

WEBB S, SUTCLIFFE J, BURKINSHAW L and HORSMAN A 1987 Tomographic reconstruction from experimentally obtained cone-beam projections *IEEE Trans. Med. Imaging* **MI-6** (1) 67–73

ZONNEVELD F W 1979 *Computed Tomography* (Eindhoven: Philips Medical Systems)